

https://dspace.org/

Internal fields in diamond and related materials

Connell, Simon Henry

2015-02-13
http://hdl.handle.net/10539/16997

Downloaded from a DSpace repository. https://dspace.org/

Ib has less nitrogen but this is on singlet substitutional sites and is paramagnetic. The type IIa has again less nitrogen and its lattice exhibits mosaic spread. The type IIb diamond is the purest. Some of the boron acceptors are not compensated and this material is naturally p-type semi-conducting. Tables 2 and 3 of Paper 3 in the Results and Conclusions section display these impurity concentrations.

Diamonds graphitize in high vacuum at 1800 K and their heat capacity at room temperature is about 6.2 J/gK. From this value the "melt energy" per atom is roughly 1.4 eV/atom. The activation energy for the diffusion of self interstitials is $\approx$ 1.3 eV [Pa 61], and they become mobile from room temperature. The vacancy in diamond is believed to be immobile until about 700°C [Lo 78]. The band gap is about 5.5 eV. A comprehensive review of diamond properties is to be found in reference [Fi 79].

Recoil implantation

Implanted ion doses and ranges

This section investigates the recoil implantation profile of the ^{19}F ions into diamond by the 4 MeV p^+ beam. The proton beam strikes a 30 $\mu g/cm^2$ layer of CaF_2 which is deposited onto the cleaned diamond surface by evaporation. Since the density of CaF_2 is 3.18 g/cm^2, the thickness of the probe-containing layer is typically 0.1 μm. Recoil implantation thus produces three species in the diamond target, the beam protons, the fluorine ions and the calcium ions. The implantation profiles of all these species must be evaluated in order to describe the environment of the ^{19}F probe ions.

In order to accumulate the required statistics in the TDPAD spectrum, each TDPAD experiment required about 30 hours of beam time. The averaged proton beam current on target was 5 nA, with a 6 mm diameter beam spot size. This gives an accumulated dose of implanted protons of 10^{16} ions/cm^2. Precise evaluation of recoil implantation profiles produced by this proton fluence remains an unsolved problem of physics, though there are several approximate numerical methods for evaluating it [Mo 75, Mo 76, Fi 78, Gr 81]. A simple model is presented to predict the implantation profiles of the ^{19}F recoil implanted fluorine, together with the fraction of ^{19}F that is excited to the 197 keV isomeric state, based on the schematic diagram in Fig. 2.1.

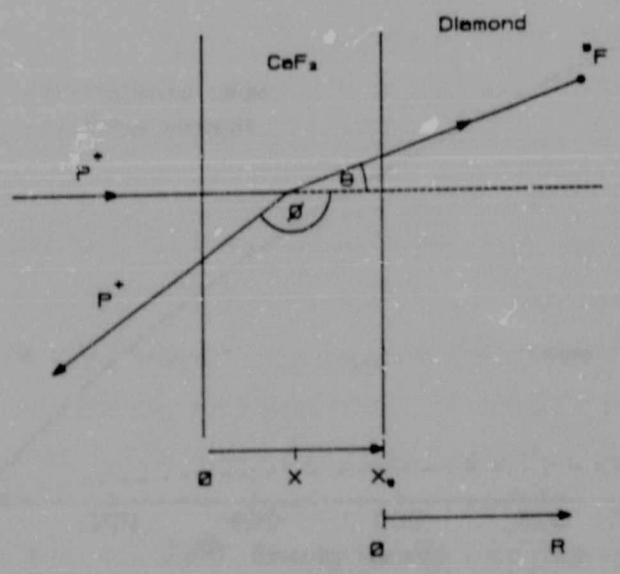


Fig. 2.1 Schematic diagram of ^{19}F recoil implantation into diamond by a p^+ beam.

We consider only primary collisions described by a $1/r^2$ potential. This is considered a good approximation in the (E, Z_1, Z_2) regime of the proton implantation in this case [Wi 70], and it leads to an elastic Rutherfordian differential cross-section which is regarded here as producing the maximum yield of implanted ^{19}F. Recent measurements [Ou 86] have shown that the Rutherford cross section estimates the experimental elastic yield accurately for projectile center of mass angles of 0°- 90° and underestimates up to a factor of 2 at larger angles. More sophisticated models have considered potentials with higher moments and also the cascade generation, and have used Monte Carlo techniques [Go 86, Ya 87]. This affects mainly the shape of the profiles. In addition, no effects such as layer deterioration by sputtering, dose dependence or an interface barrier have been included. The ^{19}F range distribution along the trajectory at the recoil angle θ is approximated by a Gaussian. The projected range $R_p(E)$ and range straggle $\Delta R(E)$ for ^{19}F in diamond are shown in Fig. 2.2. These curves were obtained with the TRIM-86 computer code [Zi 85]. For all the TRIM Monte Carlo simulations discussed below, the displacement energy for diamond E_d was taken as 55 eV, the binding energy as 5 eV and the surface energy as 2 eV [Pr 85].

For ease of computation $R_p(E)$ and $\Delta R(E)$ were parameterized with a quartic

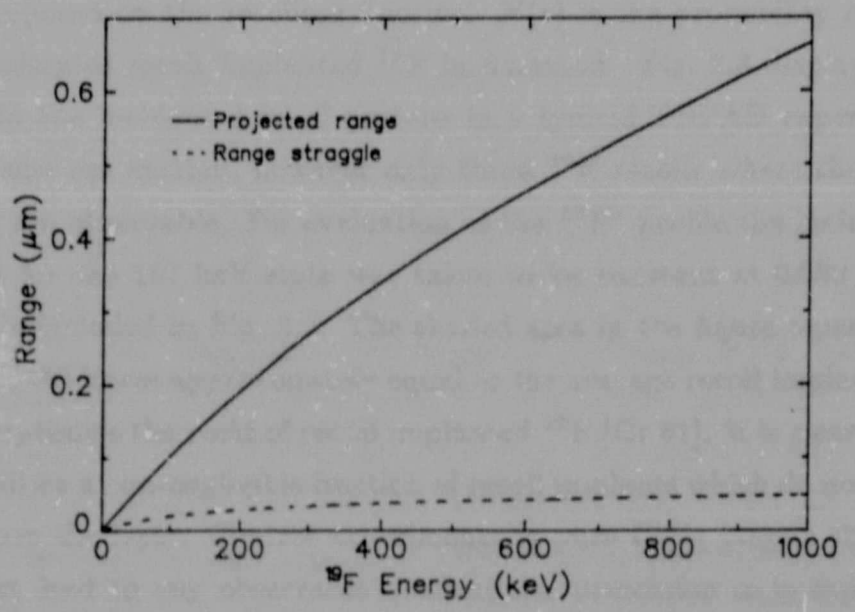


Fig. 2.2 Projected ranges and range straggle of ^{19}F in diamond.

polynomial. Kinematic considerations gave the energy of the recoiling fluorine $E(\theta)$ and the proton backscattered angle $\phi(\theta)$ as a function of the recoil angle θ. These relationships were derived from pure elastic scattering, as the effect of the fluorine being excited to the 197 keV level affects them by only 3%, since it is the recoiling proton that finances this process. The ^{19}F profile along a trajectory is then projected onto the depth axis R. This gives the implantation profile for each incident proton as

$$N(r,\theta,x) = n_a \cdot \frac{d\sigma_R}{d\Omega}[\phi(\theta)] \cdot G[R, \Delta R(E(\theta))\cos(\theta), R_p(E(\theta))\cos(\theta) - (x_0 - x)]$$

where n_a is the number of ^{19}F ions per unit area and G is a Gaussian. Since the depth of the implantation profile is of the order of the CaF_2 layer thickness, it is necessary to average over the depth of the collision x within the layer. This procedure affects only the Gaussian and can be done analytically.

$$\begin{aligned} N(r,\theta) &= < N(r,\theta,x) >_x \\ &= n_a \cdot \frac{d\sigma_R}{d\Omega} \cdot \frac{1}{2x_0}\left[\mathrm{erf}\left(\frac{R - R_p\cos(\theta) + x_0}{\sqrt{2}\sigma\cos(\theta)}\right) - \mathrm{erf}\left(\frac{R - R_p\cos(\theta)}{\sqrt{2}\sigma\cos(\theta)}\right)\right]. \end{aligned}$$

The remaining integration

$$N(r) = < N(r,\theta) >_\Omega$$

over all recoil angles was done numerically using an 8-panel Newton-Cotes adaptive quadrature [Fo 77]. To simulate the ^{19}F bound in the CaF_2 lattice an energy cut-off of 20 eV was imposed on the recoiling fluorine. $N(r)$ is the probability density function which approximates recoil implanted ^{19}F in diamond. Fig. 2.3 displays this function normalized to the incident dose of protons in a typical TDPAD experiment. Clearly not all ^{19}F ions are excited, however only those ^{19}F recoils where the 197 keV state is populated are observable. For evaluation of the $^{19}F^*$ profile the inelastic differential cross section for the 197 keV state was taken to be constant at 0.030 mb/st [Th 67]. This profile is included in Fig. 2.3. The shaded area in the figure represents the CaF_2 layer. A layer thickness approximately equal to the average recoil implantation depth is expected to optimize the yield of recoil implanted ^{19}F [Gr 81]. It is clear from the figure that there will be a non-negligible fraction of recoil implants which do not have sufficient energy to leave the layer. Control experiments in pure CaF_2 targets showed that such recoils do not lead to any observable quadrupolar precession as is expected. Fig. 2.3 clearly illustrates the reason for the recent intense interest in recoil implantation. Due to the angular dependence of the recoil cross section, this method of doping can produce extremely high doses of shallow implants. This is beneficial for device miniaturization.

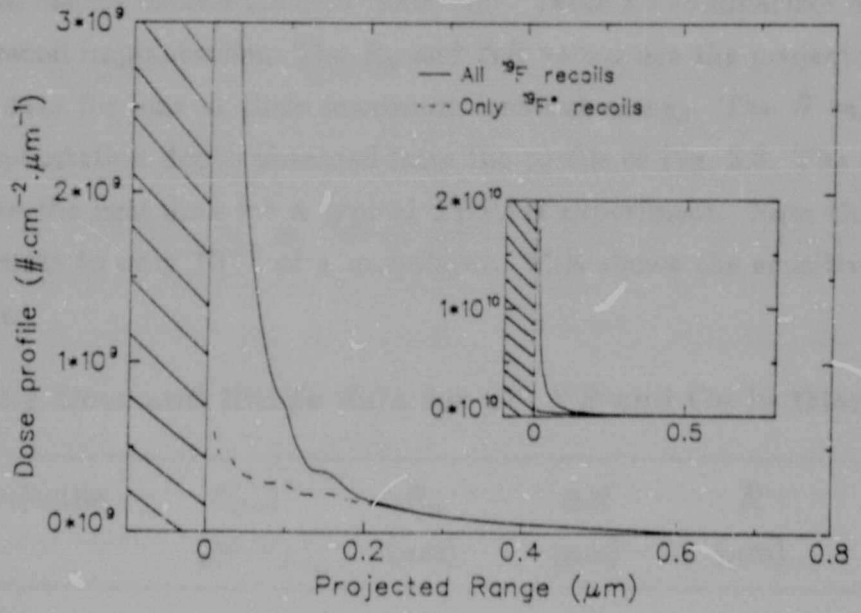


Fig. 2.3 ^{19}F recoil implantation profile.

A rough check on these calculations is given by the experimentally measured count rate of a typical TDPAD experiment. This was usually 120 Hz after correction for background. The area under the $^{19}F^*$ profile of Fig. 2.3 from a depth of 20 Å onwards is $\approx 1 \times 10^8$ probes/cm^2. With a beam spot size of 6 mm in diameter and typical count time of 30 hrs this averages $\approx$ 300 active probes in the diamond per second. Since the solid angle subtended by the detectors is 0.1 st and since this is a singles counting experiment where most of the $^{19}F^*$ has decayed during each count cycle, the theoretical count rate is 30 Hz. This agreement is satisfactory considering the simplicity of the approximations and the fact that some ^{19}F probes are excited but do not enter the diamond substrate. Note that the profile in Fig. 2.3 justifies interpreting the ^{19}F as a bulk probe since the surface of the diamond may be taken as no more than 20 Å thick (6 lattice constants) for the purposes of these experiments. The Ca recoil implantation will follow a qualitatively similar curve to the ^{19}F. However, there is only half as much Ca in the evaporated layer and kinematics show that it will receive 50% less kinetic energy from the recoil. In addition, the stopping power for Ca is approximately 2 - 5 times that of ^{19}F in these energy ranges. Thus the Ca recoil implantation profile will be shallower and at less than half the dose of the ^{19}F profile. The total dose of Ca and ^{19}F impurities cannot exceed 1.5×10^8 ions/cm^2. Table 2.1 summarizes all the ballistic data for ^{19}F recoil implantation. The R_p and ΔR values are the projected range and range straggle data for ions at their maximum incident energy. The $\bar{R}$ value is the averaged recoil implantation depth obtained from the profile of Fig. 2.3. The implantation doses pertain to the nett dose for a typical TDPAD experiment. Note that the nett dose of ^{19}F amounts to only 10^{-7} of a monolayer. This shows the sensitivity of the TDPAD technique.

Table 2.1 Dose and Range data for p^+, ^{19}F and Ca in Diamond

Projectile	E_{max} (MeV)	R_p (μm)	ΔR (μm)	$\bar{R}$ (μm)	Dose (ions/cm^2)
p^+	4.0	76	2.8	-	10^{16}
^{19}F	.76	.525	.045	.02	10^9
$^{19}F^*$	.74	.51	.044	.14	10^8
Ca	.38	.174	.024	-	$.5 \times 10^8$

TDPAD time window

The TDPAD technique (with ^{19}F as probe ion) measures only during a time window of about 10 - 500 ns immediately following each recoil implant. It can be considered what sort of effects are possible in this time span. The slowing down time of the ^{19}F is of the order of 1 ps. Migration of the ^{19}F away from the point where it has stopped or the recombination of Frenkel pairs more than 1 lattice site from each other are expected to be diffusive processes in the local temperature regime of this experiment (see the following section). The time for self-interstitial diffusion across one lattice site can be used to approximate the time taken for both processes. The activation energy for self interstitial diffusion is $\approx$ 1.3 eV and the jump frequency is $\approx 10^{13}$ Hz [Pa 61]. Thus the self-interstitial diffusion time across one lattice site is $> 10\,\mu s$ for even the highest temperature (800 K) measured in these experiments. The time window thus amounts to a "snapshot" of the ^{19}F taken directly after recoil implantation. This rules out trapping effects and mobility effects which are important for the more general PAC experiments.

Radiation damage environment

The body of information on radiation damage in metals is much more mature than in insulators or semi-conductors. In metals there is usually less radiation damage as the metals are self annealing, largely due to the lack of directed bonds and the higher mobility of interstitials due to the higher lattice pressure. In addition the band structure of semi-conductors complicates analytical treatments. However it is still important to investigate in general terms the situation for ^{19}F in diamond, as this relates to the interpretation of the TDPAD spectra. In evaluating the radiation damage environment of the ^{19}F probes, a normally incident ^{19}F probe atom with an energy of 400 keV was taken as representative. The full expressions which average over all incident angles are considered to be unnecessary for the present purposes.

The question arises as to whether the temperature in a single cascade volume is sufficient to cause local melting of the lattice which could result in amorphized or recrystallized regions. It was previously estimated that in diamond this required an energy deposition of $\approx$ 1.4 eV/atom by the recoiling probe ion. Calculating the cascade energy density requires a knowledge of the cascade dimensions. The

longitudinal dimensions of the cascade are approximated by the TRIM range profile. Two methods have been used to evaluate the lateral dimensions of the cascade. An order of magnitude extrapolation based on the graphed results of transport calculations for ^{19}F in amorphous carbon with the density of diamond gives a lateral straggling of $\sigma_\perp = 0.06\,\mu m$ [Z1 85a]. Transport calculations based on the m=$\frac{1}{2}$ power law approximation to the Thomas-Fermi potential give $< Y^2 > / < X >^2 = 0.107$ for the lateral straggling to range ratio for mass ratios of $M_{tgt}/M_{ion} = M_C/M_F$ [Wi 70]. This gives $\sigma_\perp = 0.1\,\mu m$ which will be an over estimate since a higher power approximation to the T-F potential is more appropriate for 400 keV ^{19}F in diamond. Thus $\sigma_\perp = 0.06\,\mu m$ was chosen for the calculations on the volume of the collision cascade which follow. Fig. 2.4 shows the TRIM calculation of the electronic and nuclear components of the stopping of 400 keV ^{19}F ions in diamond.

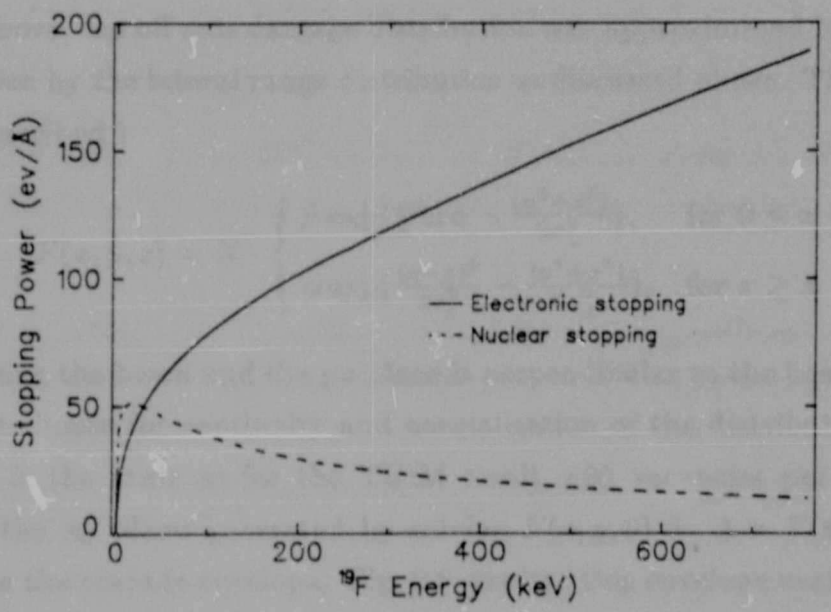


Fig. 2.4 Electronic and nuclear stopping powers for ^{19}F in diamond.

The defects in the lattice will be caused predominantly by the nuclear stopping component since the primary energy loss is through a cascade of elastic collisions. The "dimensions" of the cascade are thus calculated from the nuclear (recoil) loss envelope [Da 83]. The TRIM prediction of the energy deposited in this envelope is 12.5% of

the incident ^{19}F energy. From the figure it is clear therefore that most of the damage will be concentrated near the end of the ^{19}F track, where the ^{19}F has less energy and the nuclear stopping component is largest. Fig. 2.5 shows the relationship between the damage distribution and the range distribution for a single cascade produced by averaging many Monte Carlo simulations of such cascades by the TRIM program. The bold line is an approximation to the longitudinal projection of the cascade produced from a leading Gaussian component and a trailing exponential component. No attempt was made to fit the bold curve to the TRIM data; instead the average range and longitudinal range straggle were taken as acceptable parameters for the Gaussian approximation to the deepest part of the damage distribution and the shallow exponential part is parameterized for matching of the TRIM damage distribution near the surface. In order to generate a three dimensional cascade envelope from the longitudinal projection described above, the off axis damage distribution was approximated by a Gaussian with a spread given by the lateral range distribution as discussed above. The cascade volume was thus described by

$$F(x,y,z) = N \cdot \begin{cases} \beta \exp\left(\frac{x}{\bar{x}} \ln a - \frac{(y^2+z^2)}{2\sigma_\perp^2}\right), & \text{for } 0 \le x < \bar{x} \\ \alpha \exp\left(\frac{(x-\bar{x})^2}{2\sigma_\parallel^2} - \frac{(y^2+z^2)}{2\sigma_\perp^2}\right), & \text{for } x \ge \bar{x} \end{cases}$$

Here x is along the beam and the yz plane is perpendicular to the beam. The constants α and β are chosen for continuity and normalization of the distribution to unity. The value of N is the same as for the TRIM result, 490 vacancies per cascade. A 10% contour in the xy plane generated by solving $F(x,y,0) = .1 \times F(\bar{x},0,0)$ is taken to approximate the cascade envelope. Fig. 2.6 displays this envelope evaluated for 400 keV ^{19}F in diamond. Also shown is a single representative Monte Carlo cascade calculated by TRIM.

An integration gives the volume of this cascade envelope as $.015\,\mu m^3$. There are obvious difficulties in associating an average cascade volume as calculated from the transport equation with the cascade volume due to an individual ion [Da 83]. A volume correction factor V_R has been introduced [Wa 78]. For the mass ratio of ^{19}F in diamond this is $V_R \approx .27$. The deposition of the nuclear stopping energy loss, 12.5% of 400 keV, in this adjusted volume and $N = .176$ atoms/Å^3 for the number of carbon atoms per unit volume gives the deposited energy density $\theta \approx 2 \times 10^{-5}$ eV/atom.

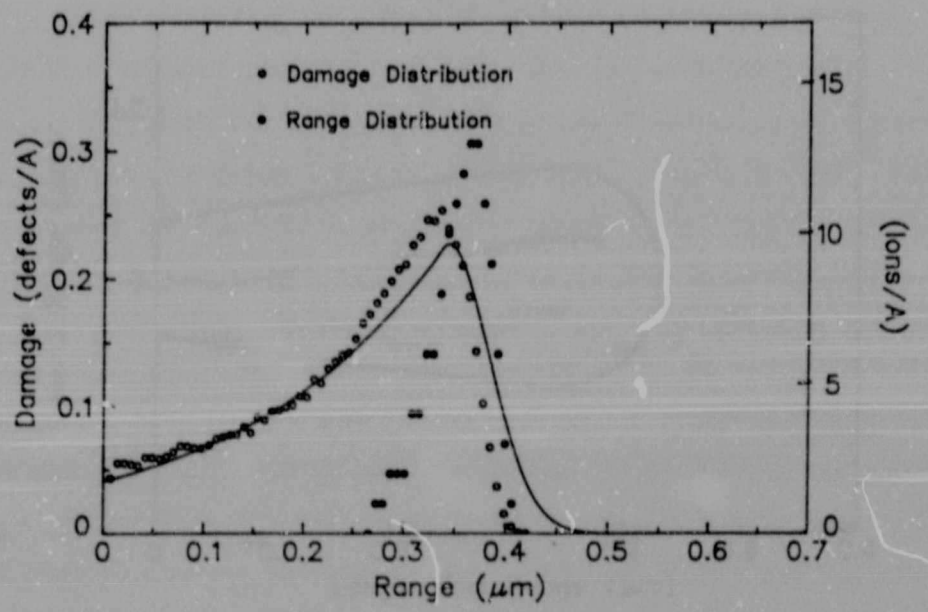


Fig. 2.5 Relation between damage and range distributions for 400 keV ^{19}F in diamond. The solid line is the longitudinal projection of the damage distribution model.

Working directly from WSS theory [Wi 70] on the gross spatial distribution of energy through elastic-collision cascades, Sigmund [Si 74] has provided contour plots of the factor G_2 in the expression $\theta = G_2 N^2 / E_{inc}^2$ which gives a first approximation to the mean energy deposited per atom. For 400 keV ^{19}F in diamond this also gives $\theta \approx 2 \times 10^{-5}$ eV/atom. The time taken to establish this energy density is the slowing down time of the ion in the target [Si 74]. In the case of ^{19}F in diamond this is $\approx$ 1 ps. Any other thermal processes can only lower the the value presented here. Clearly no thermal spike effects involving thermal amorphization or recrystallization are possible, since this requires energy densities of the order of 1 eV/atom [Da 83]. Any amorphization process will be the result of an aggregation of defects [Ca 82]. In addition the recombination of Frenkel Pairs is not assisted by the local energy density and all movement of interstitials after implantation will be diffusive.

Calculating the number density of primary defects (FP's) in the cascade envelope (Fig. 2.6) from the TRIM prediction of 490 vacancies per ion gives an average of a mere $\approx 3 \times 10^{-8}$ vacancies/Å^{3}ion. Of course this defect density is slightly higher in the

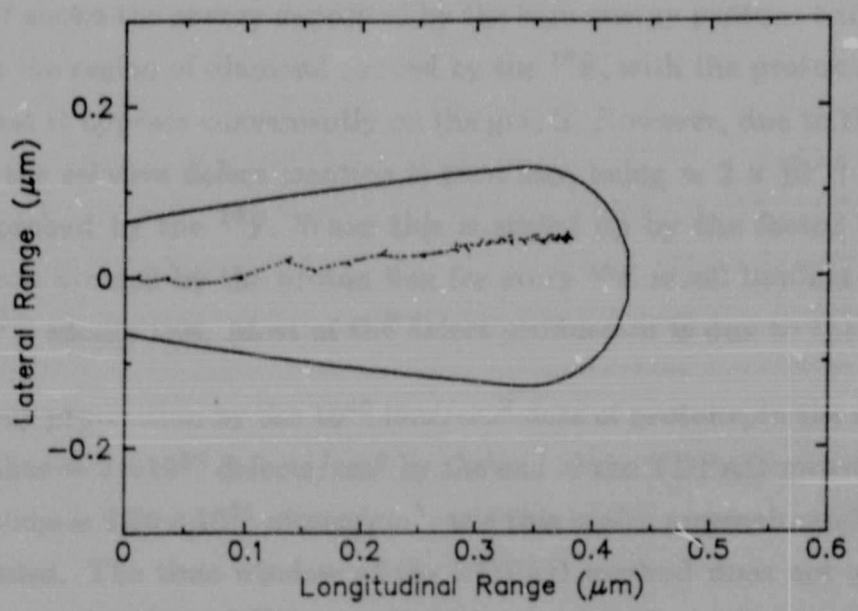


Fig. 2.6 Approximate 10% averaged cascade envelope for 400 keV ^{19}F in diamond. An individual Monte Carlo TRIM simulation is included.

deepest regions of implant. Since the nett ^{19}F dose in the probe area is only 10^{-7} of a monolayer each ^{19}F probe may be considered independent of the other ^{19}F ions in the diamond. Even as the TDPAD experiment progresses, the damage will not build up substantially, since at the dose of 10^9 ^{19}F ions/cm^2, the envelope of Fig. 2.6 contains only 200 individual cascades. Similar reasoning applies to the damage due to the Ca ions, though this is not as deep.

The protons stop almost 500 times deeper than the average depth region probed by the ^{19}F. However the proton will still deposit energy in this region as it passes through, and this effect must be evaluated. It is unlikely that any protons involved in a recoil will be in this region since they lose less than 25% of their energy and will still vacate the area probed by the ^{19}F. The electronic and nuclear stopping powers of the proton are approximately constant at 3.0 eV/Å and 5×10^{-3} eV/Å respectively, in the relatively shallow region probed by the ^{19}F where the proton does not lose much energy. Again it is the nuclear stopping component that leads to the creation of defects and here the electronic contribution is clearly dominant. However there are 10^7 protons transmitted through this region for each ^{19}F recoil implant. This fact should be accounted for in

the comparison of the damage created by the ^{19}F probe ion with that created by the proton. Fig. 2.7 shows the energy deposited by the high energy protons and the recoiling fluorine only in the region of diamond probed by the ^{19}F, with the proton's value scaled up by 10^4 so that it appears conveniently on the graph. However, due to the small mass of the proton, the relative defect creation is even less, being $\approx 2 \times 10^{-6}$ defects/Å ion in the region probed by the ^{19}F. When this is scaled up by the factor 10^7 there are about 200 defects created by the proton flux for every ^{19}F recoil implant in the region of maximum ^{19}F energy loss. Most of the defect production is due to the proton.

The vacancy production by the 10^{16} ions/cm^2 dose of protons, in the region probed by the ^{19}F, is thus $\approx 2 \times 10^{18}$ defects/cm^3 by the end of the TDPAD measurement. The density of C-atoms is 1.76×10^{23} atoms/cm^3, and this is also approximately the number of interstitial sites. The time window of the TDPAD method does not allow any ^{19}F diffusion, so the probability of ^{19}F stopping in a vacancy from the proton predamage is 10^{-5}. Unless there are other processes operating, a large fraction of substitutional residence sites for the ^{19}F implanted impurity is thus not expected.

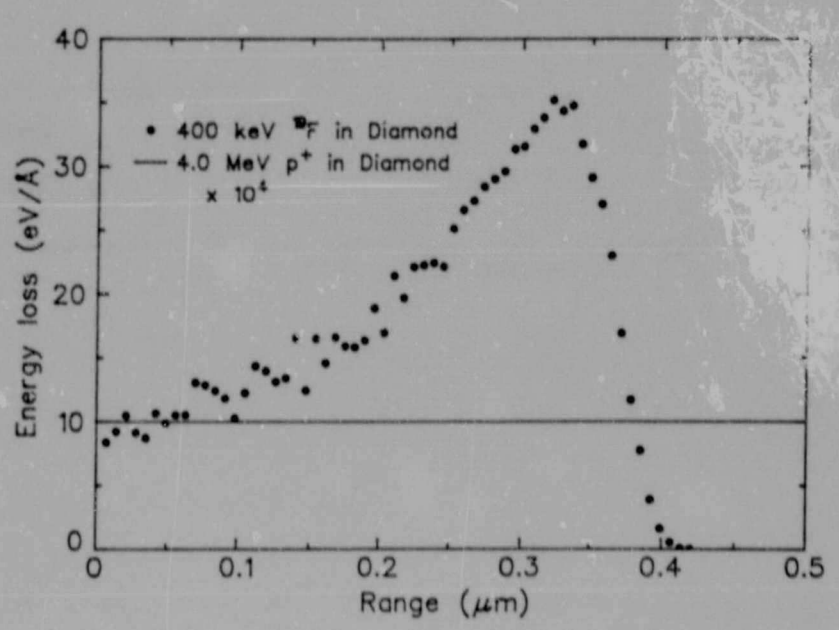


Fig. 2.7 The energy deposited by p^+ and ^{19}F in diamond, in the region probed by the ^{19}F.

Summary

In this section the TDPAD method with ^{19}F recoil implantation in diamond was discussed. The important results are the recoil implantation profile of Fig. 2.3 for $^{19}F^{*}$. It was found that these experiments operate five orders of magnitude below the thermal spike context. This means that diffusive processes are dominant, allowing the TDPAD measurement to be interpreted as a "snapshot" taken immediately after recoil implantation and long before any carbon or ^{19}F diffusive motion has occurred. The damage environment was found to be minimal, even including the effects of the proton pre-damage. Finally, note that the ^{19}F probe is blind beyond two lattice site's distance due to the TDPAD time window and the insensitivity of the quadrupole interaction to effects much beyond the nearest neighbour environment.

CHAPTER 3.
THEORETICAL (TDPAD)

Contents

Perturbed Angular Distributions 34

Angular correlations 34

^{19}F Angular distribution 36

Adding the perturbation 38

The Electric Field Gradient 40

Single Crystal Formalism 42

Explicitly for $I = \frac{5}{2}^+$ 44

Simulations 44

Perturbed Angular Distributions

Angular correlations

This derivation of the angular correlation function mostly follows that of Frauenfelder and Steffen [Si 65] which has become the standard text on the subject. Consider a double decay cascade from an initial level of spin I_i via emission of radiation along the direction $\mathbf{k}_1$ to the intermediate level I, followed by another decay, $\mathbf{k}_2$, to the final level I_f, as shown in Fig. 3.1.

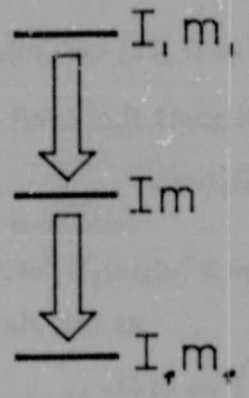


Fig. 3.1 Double decay cascade.

An expression is sought for the directional correlation function $W(\mathbf{k}_1, \mathbf{k}_2)$ where $W(\mathbf{k}_1, \mathbf{k}_2)d\Omega_1 d\Omega_2$ gives the probability for detecting the second radiation in the direction $\mathbf{k}_2$ in $d\Omega_2$ consecutively to the first radiation in direction $\mathbf{k}_1$ in $d\Omega_1$. By the conservation of angular momentum the emission direction of the radiations is related to the populations of the magnetic substates of the emitting level. The population of each magnetic substate of a level is completely described by the density matrix $<m|\rho|m'>$ for that level. In particular, the probability of finding the nucleus in state $|m>$, (not necessarily an eigenstate) is given by

$$P(m) = <m|\rho|m> . \tag{3.1}$$

If the transition $I_i \longrightarrow I$ is induced by the operator H_1 then the density matrix of the intermediate state is related to its precursor by

$$<m|\rho(\mathbf{k}_1)|m'> = S_1 \sum_{m_i, m_i'} <m|H_1|m_i><m_i|\rho_i|m_i'><m'|H_1|m_i'>^* \tag{3.2}$$

where S_1 indicates a sum over unmeasured properties of the radiation along $\mathbf{k}_1$, and $<m|H_1|m_i>$ stands for $<Im\mathbf{k}_1\sigma_1|H_1|I_im_i>$ where all the symbols have their usual meanings. Applying this procedure successively to the second transition, the probability that the nucleus is in the final state $|m_f>$, providing the first radiation was along $\mathbf{k}_1$ and the second was along $\mathbf{k}_2$, is found to be

$$\begin{aligned} P_f(m_f) &= <m_f|\rho(\mathbf{k}_1,\mathbf{k}_2)|m_f'> \\ &= S_1S_2 \sum_{m_i,m_i',mm'} <m_f|H_2|m><m|H_1|m_i><m_i|\rho_i|m_i'> \\ &\quad \times <m'|H_1|m_i'>^*<m_f'|H_2|m'>^* . \end{aligned} \tag{3.3}$$

This expression is simplified, assuming the initial state is randomly aligned,

$$<m_i|\rho_i|m_i'> = (2I_i+1)^{-1}\delta_{mm'}. \tag{3.4}$$

Since the density matrix ρ_f would have unit trace if $(\mathbf{k}_1,\mathbf{k}_2)$ were always observed,

$$\begin{aligned} W(\mathbf{k}_1,\mathbf{k}_2) &= S_1S_2 \sum_{m_fmm'm_i} <m_f|H_2|m><m|H_1|m_i> \\ &\quad \times <m'|H_1|m_i>^*<m_f|H_2|m'>^* . \end{aligned} \tag{3.5}$$

A typical matrix element above evaluates as

$$\begin{aligned} <m|H|m_i> &= \sum_{L\pi M\mu} (-1)^{-I+L-m_i} \begin{pmatrix} I & L & I_i \\ m & M & -m_i \end{pmatrix} \\ &\quad \times <0\sigma|L\mu\pi><I \parallel L\pi \parallel I_i> D^{L*}_{M\mu}(z\to\mathbf{k}) \end{aligned} \tag{3.6}$$

where $LM\pi$ are the angular momentum quantum numbers of the radiation, and D is the rotation matrix for the $(z\to\mathbf{k})$ rotation that specifies the direction of $\mathbf{k}$ with respect to an arbitrary system. Clearly the correlation $W(\mathbf{k}_1,\mathbf{k}_2)$ can be written as the product of factors dependent on the level spins and radiation multipolarities, and an angular part. Thus when the only the angle between $\mathbf{k}_1$ and $\mathbf{k}_2$ is observed (directional correlations), and the radiation polarizations are not observed,

$$W(\theta) = \sum_{k\ \text{even}} A_k(L_1L_1'I_iI)A_k(L_2L_2'I_fI)P_k(\cos\theta). \tag{3.7}$$

The internal structure of the A_k coefficients is displayed by carefully following the substitution of the typical matrix element (3.6) above into the correlation expression (3.7). Tables exist evaluating these coefficients for many cases [Si 65a]. The highest term in the expansion is given by selection rules which for our case of pure multipole radiation gives

$$0 < k < \text{Min}(2I, 2L_1, 2L_2) = k_{\max}. \tag{3.8}$$

^{19}F Angular distribution

The difference between the ^{19}F angular distribution and the angular correlation of a double γ cascade is clarified by Fig. 3.2 below. The theoretical treatment is similar if $I_i = I_f = I_{gs}$. The transition feeding the intermediate state is replaced by the nuclear reaction ^{19}F(p,p')^{19}F*, which in this case produces the alignment of the intermediate state leading to the spatial anisotropy of the de-excitation radiation.

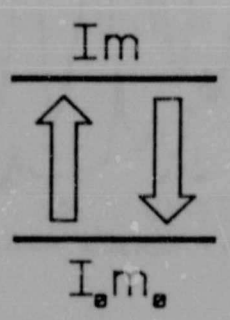


Fig. 3.2 ^{19}F excitation and decay.

Fig. 3.3 shows the cross section for excitation of the 197 keV state of ^{19}F via the reaction ^{19}F(p,p')^{19}F*. For historical reasons our experiments were performed with the p^+ projectile energy of 4 MeV. This is well above the Coulomb barrier which is at 2.826 MeV. The Coulomb excitation cross section [Al 54] calculated with the reduced transition matrix element $B(E2) = 5 \times 10^{-3}$ e$^2\times$ barns^2 [St 60] contributes only 0.3% to the total inelastic cross section at this energy. The coefficients for the de-excitation transition for the ^{19}F* case are given by tables [Si 65a]

$$A_2(2) = -.5345$$
$$A_4(2) = -.0267 \qquad (3.9)$$

where the (2) denotes the second transition. Note that $k_{max} = 4$ for this case. The $A_k(1)$ coefficients for the feeding transition are no longer simply available from tables, and they must be measured or devised by other methods. Two methods have been used to determine these coefficients for the feeding transition. If all the alignment of the $\frac{5}{2}^+$ state is well described by Coulomb Excitation (CE) theory, then the coefficients for the electric quadrupole CE case are [Al 53]

$$A_k^{CE}(1) = A_k^7(1)a_k(\xi) \qquad (3.10)$$

Author Connell S H
Name of thesis Internal Fields in Diamond and Related Materials 1988

PUBLISHER:
University of the Witwatersrand, Johannesburg
©2013

LEGAL NOTICES:

Copyright Notice: All materials on the University of the Witwatersrand, Johannesburg Library website are protected by South African copyright law and may not be distributed, transmitted, displayed, or otherwise published in any format, without the prior written permission of the copyright owner.

Disclaimer and Terms of Use: Provided that you maintain all copyright and other notices contained therein, you may download material (one machine readable copy and one print copy per page) for your personal and/or educational non-commercial use only.

The University of the Witwatersrand, Johannesburg, is not responsible for any errors or omissions and excludes any and all liability for any errors in or omissions from the information on the Library website.